Cement and Concrete Research 135 (2020) 106149

Contents lists available at ScienceDirect

Cement and Concrete Research

journal homepage: www.elsevier.com/locate/cemconres

Thermodynamic study of cement/rock interactions using experimentally generated solubility data of zeolites

Bin Ma[a,*], Barbara Lothenbach[a,b]

[a] Laboratory for Concrete & Construction Chemistry, Swiss Federal Laboratories for Materials Science and Technology (Empa), 8600 Dübendorf, Switzerland
[b] Department of Structural Engineering, Norwegian University of Science and Technology (NTNU), 7491 Trondheim, Norway

ARTICLE INFO

Keywords:
Degraded cement/rock interface
Zeolite
Solubility product
Thermodynamic data
Cemdata
Stability domain
Nuclear waste disposal

ABSTRACT

Alteration of widespread interfaces between cements and clays in geological time scales is essential to the safety assessment of radioactive waste repositories but not well understood partly due to the low reliability of thermodynamic data for zeolites. Here, we collected and full-scale characterized Ca-based zeolites with six types of frameworks that could possibly form in the interfaces. Besides, chemical interactions between degraded cementitious phases and rock forming minerals after equilibrating for ~6 years were investigated. By using the currently generated thermodynamic data of selected zeolites, chemical interactions in the cement/rock systems were studied, showing that no equilibrium was reached after 6 years and zeolites favored in thermodynamics, such as chabazite and gismondine rather than faujasite, can be expected to form at even longer timescale. The experimentally derived thermodynamic data was verified preliminarily by establishing consistent predominance diagrams of cement-zeolite-clay minerals, helping to predict zeolite stability domains in large timescales.

1. Introduction

Large quantities of cementitious infrastructures are foreseen in clay-rich nuclear waste repositories, for waste matrix, canisters, backfill, and tunnel support [1,2]. Thus, interfaces between cements and clays are expected to exist universally in repositories. The safety of such geological repositories should be guaranteed on a geologic time scale. Over this long period, hydrated Portland cement will undergo four main degradation stages: i) 13.5 > pH > 12.5, release of alkalis (i.e., Na^+ and K^+); ii) pH = 12.5, dissolution of portlandite; iii) 12.5 > pH > 10, dissolution of low Ca/Si calcium (alumino)silicate hydrates (C-(A-)S-Hs) and aluminoferrite minerals; iv) pH = incoming water solution, dissolution of calcite [3–5]. After thousands of years, C-(A-)S-Hs and aluminoferrites (e.g., AFm phase, ettringite, and katoite) would predominate the degraded cement for many more millennia [5–8]. Together with the alkalis released initially from the cement and the aluminosilicate minerals in the adjacent rock, the chemical environment will facilitate the formation of secondary minerals. The potential products of cement-clay interaction could include C-(A-)S-Hs, zeolites, hydroxides, carbonates, polymorphs of silica, and some sheet silicates [9–11]. Thus after the long period before any leaching of nuclear waste can be expected, the potential retarders for radionuclides could be rather the degraded cementitious phases than the actual cement [12].

The interactions of a simplified, degraded Portland cement (PC)/rock system were simulated and investigated experimentally at 20, 50 and 80 °C in our previous work [13]. Among the reaction products, several types of naturally occurring zeolites, such as natrolite, chabazite, gismondine, and faujasite, were detected to form experimentally. Both experimental and modelling studies have indicated that secondary zeolitic minerals can have important roles in controlling the geochemical environment and its spatial and temporal evolution [9,13,14]. For assessing the evolution of the geochemical environment within a repository in a geological time scale, thermodynamic prediction based on reliable thermodynamic properties of zeolites is the only feasible approach. However, some of the experiment-derived solubility products of zeolites were significantly different to the estimated and measured values in literatures, and re-evaluation of the few measured values in literatures showed largely diverging values. The significant differences (several log units) in solubility products of zeolites are partly caused by the high structural variations of Al/Si ratios and extra-framework cations [13–15] and kinetics of precipitation/dissolution in case of equilibration experiments.

Given the large number of zeolite types and compositions that may be considered in a safety assessment, researchers tried developing “critical and systematic” selection strategies and empirical estimation methods on thermodynamic data of zeolites. Consequently, the polymer model [14,16] and the additivity method [17,18] were developed to calculate the thermodynamic data, such as the standard Gibbs free

* Corresponding author.
E-mail address: bin.ma@empa.ch (B. Ma).

https://doi.org/10.1016/j.cemconres.2020.106149
Received 22 January 2020; Received in revised form 6 April 2020; Accepted 1 June 2020

energy of formation (ΔG_f^0), the standard enthalpy of formation (ΔH_f^0), the standard entropy (S^0), and the standard heat capacity (C_p^0), based on elementary (hydro)oxide components. These estimation methods have been shown to provide reasonably satisfactory results if compared to experimental values from calorimetry measurements [14,19,20]. Via comparing and selecting both the measured and estimated thermodynamic data (including solubility product (K_{sp}), ΔG_f^0, ΔH_f^0, S^0, and C_p^0) of zeolites [21], several mainstream thermodynamic databases (e.g., databases of ThermoChimie [22], LLNL.dat [23], Slop07.dat [24], and Phreeqc.dat and Wateq.dat [25]) have presented quite complete zeolite thermodynamic dataset. However, the conversion from measured S^0 and ΔH_f^0 to log K_{sp} may introduce additional errors and differences, which may be large enough to cause unreasonable thermodynamic predictions (in particular due to the large difference in ΔG_f^0 and ΔH_f^0 of Al^{3+} between different databases as well as the large measurement error for ΔH_f^0). In contrast, solubility measurement on fine and pure zeolite powders can be a comparatively direct method to evaluate the log K_{sp} values more directly and further the thermodynamic properties of zeolite minerals [26].

The consistency between the thermodynamic data generated by solubility measurements, calorimetry measurements, and prediction models was carefully verified for analcime, mordenite, and clinoptilolite [21]. It showed that the predictions (mostly based on calorimetry measurements) matched tightly with the solubility data for analcime [26]. In contrast, for both mordenite and clinoptilolite [26,27], a good agreement was observed only at temperatures higher than 100 °C but not below 100 °C. Further verifications were limited to the scarcity of solubility data reported. In addition, kinetic barriers hinder the precipitation of several zeolites, such as natrolite, gismondine or analcime at ambient temperature, while others, e.g. faujasite, form readily at ambient temperatures [9]. These factors together make the determination of thermodynamic data for zeolites a considerable challenge both experimentally and in terms of defining appropriate solid solution. The limited solubility data of zeolites reported in literatures and the possible log K_{sp} discrepancy introduced by the conversion from calorimetry data underline the need for a systematic experimental determination of the solubility products for different zeolites.

In this study, we continued to explore the chemical interactions between the degraded PC phases and rocks after equilibrating for ~6 years, in order to investigate the possible equilibrium state of the system via thermodynamic modelling. Motivated by the zeolite formation in the simulated degraded PC/rock system and the limited solubility data of zeolites in literatures, we aim to determine the thermodynamic properties of zeolites systematically and experimentally based on solubility products at different temperatures. Currently, Ca-based zeolites with six types of aluminosilicate frameworks, i.e., chabazite with CHA framework (CHA(Ca)), gismondine low-silica P with GIS framework (LS-P(Ca)), mordenite with MOR framework (MOR (Ca)), scolecite with NAT framework (SCO), stilbite with STI framework (STI), and heulandite and clinoptilolite with HEU framework (HEU_1, HEU_2, and CLI), were studied. Together with a parallel study on Na-based zeolites (including analcime (ANA), gismondine low-silica P (LS-P(Na)), phillipsite (PHI(Na)), chabazite (CHA(Na)), faujasite (FAU-X and FAU-Y), natrolite (NAT), and mordenite (MOR(Na))) [28], zeolites that could possibly form in chemical environments of long-term underground concrete constructions were investigated. By using the experimental thermodynamic data of zeolites initially generated here, we aim to predict the stability domains of zeolites and to better understand the zeolite formation process during cement/rock interactions.

2. Materials and methods

2.1. Materials

Sodium aluminate ($NaAlO_2$, technical grade, Sigma-Aldrich) and silica fume (SiO_2, chemical grade, Aerosil 200) were used as starting materials for the degraded cement/rock interactions. $Ca(NO_3)_2{\cdot}4H_2O$ (≥99%, ACS reagent) was bought from Sigma-Aldrich and used for cation exchange. Fresh Milli-Q water (18.2 MΩ·cm) was used for all solutions and suspensions. Four types of Ca-based natural zeolites (Fig. A1), i.e., scolecite, heulandite (two different samples, labelled as HEU_1 and HEU_2), clinoptilolite, and stilbite, were collected for the determination of their thermodynamic properties. The heulandite and stilbite were originally exploited from Nasik, India, the clinoptilolite from Germany, and the scolecite from New Malden, U.K. All the natural zeolites were crushed, picked, ground by an agate mortar, and sieved with a 63-μm pore size stainless sieve.

2.2. Ca-based zeolite synthesis

Chabazite [29,30], gismondine low-silica P [31–33], and modenite [34] were synthesized via hydrothermal methods using modified recipes from the corresponding literatures. The detailed synthesis protocols were shown in our recently submitted work [28]. The necessary modifications of recipes were explored, due to the different reactivity of our raw materials with those of the materials used in literature. The Ca^{2+} endmembers of the as-synthesized zeolites were obtained by hydrothermal cation exchange method [35], using 1.0 M $Ca(NO_3)_2$ solution as the exchange solution. Typically, a solid-to-liquid (S/L) ratio of 50 g L^{-1} was used. The suspension was sealed in a Teflon vessel, and placed in an oven at 80 °C for 24 h. After exchange reaction, the suspension was centrifuged and the remaining solid was washed with Milli-Q water one time. In order to get a pure enough Ca^{2+}-endmember, this process was repeated 6 cycles. In the last cycle, the solid product was collected by vacuum filtration and was washed by Milli-Q water for 4 times to remove residual $Ca(NO_3)_2$. The filter cake was dried in an oven at 80 °C. Finally, the dried zeolites were equilibrated in a desiccator, with saturated $CaCl_2$ solution and CO_2 trap placed inside to maintain a constant 35% relative humidity and low CO_2 level, respectively.

2.3. Batch dissolution experiments

The dissolution kinetics of several Na-based zeolites have been studied at 20 °C in [28], suggesting that the dissolution equilibrium can be almost reached within 30 days. The equilibration time could also affect the solubility results, which could lead to somewhat higher solubility here. For clinoptilolite and mordenite for example, Benning et al. [27], Wilkin and Barnes [26], and Murphy et al. [36] used equilibration times up to two years at 25 °C in order to achieve equilibrium from dissolution and precipitation, although the differences in dissolution experiments were small after 3 months and longer. Here, batch dissolution experiments were conducted at 20, 50, 60, and 80 °C, in order to obtain the solubility products of Ca-based zeolites at different temperatures. Each type of zeolite was dispersed into ultrapure water with an identical S/L ratio of 50 g L^{-1}. After equilibrating for 30 days, the suspension was filtered through 0.22 μm syringe Nylon filters. Immediately, a small aliquot of the filtrate for each reactor was extracted and measured using a Knick pH meter (pH-Meter 766) and a Knick SE100 electrode. On the same days, the other portion of the filtrate was diluted with Milli-Q water if necessary and the aqueous concentrations of Na^+, K^+, Ca^{2+}, Mg^{2+}, Al^{3+}, SiO_3^{2-}, NO_3^-, and Cl^- were analyzed by ion chromatography (IC, Dionex DP series ICS-3000). The experimental detection limit of the IC was estimated to be 0.025 mg L^{-1} and the IC measurement error 5–10%.

2.4. Simulated experiments for degraded cement/rock interactions

To simulate a simplified degraded PC/rock interface corresponding to stage III degradation (see Section Introduction), where zeolites are expected to form, the corresponding predominant cement hydrates (i.e.,

C-S-H ($Ca_{0.8}SiO_{2.8}\cdot 32H_2O$) and ettringite ($Ca_6Al_2(SO_4)_3(OH)_{12}\cdot 26H_2O$)), a typical rock forming mineral (natural albite, an experimental composition of $Na_{1.33}AlO_{2.17}\cdot 0.34H_2O$, from Navarro River, Mendocino Co, California), and the common Si and Al sources (i.e., silica fume and $NaAlO_2$, respectively) for high Si and Al concentrations were selected as the starting materials in the simulated cement/rock interaction experiments. The batch experiments were set up in a N_2-filled glove box in duplicate. Each replicate included two reactors, labelled with AEC (26.5 g L^{-1} Albite +6.4 g L^{-1} Ettringite +2.0 g L^{-1}C-S-H) and AlSiE (8.3 g L^{-1} $NaAlO_2$ + 18.2 g L^{-1} silica fume +6.4 g L^{-1} Ettringite), respectively. The each two reactors were equilibrated at 50 and 80 °C, respectively, for ~6 years (2095 days). After reaction, the aqueous phase was sampled by 0.22 μm syringe filters and was measured by the pH electrode and by the IC. Besides, the solid phase were collected by vacuum filtration in the glove box. The obtained solids were dried under vacuum using freeze-drying technique to reduce carbonation degree. After drying, samples were equilibrated in a desiccator at 35% relative humidity. More experimental set-up details can be found in our previous work [13], where the reaction up to 3 years has been studied.

2.5. Solid phase characterization

The framework structures of zeolites and mineral compositions of the cement/clay specimens were identified by XRD. XRD signal was collected with a PANalytical X'Pert Pro diffractometer in a θ-2θ configuration. Oriented mounts were prepared and Co Kα radiation at 1.789 Å used. TGA was performed with a Mettler Toledo TGA/SDTA 851e on ~40 mg of sample using a heating rate of 20 °C min^{-1} from 30 to 980 °C and N_2 as protective gas. Prior to performing TGA, samples were equilibrated in the humidity- and CO_2- controlled desiccator described above for at least one week, in order to unify the adsorbed water content on all the zeolites. The elemental fractions of zeolites were characterized by energy dispersive X-ray spectroscopy (EDS) analyses, which were carried out with a Philips ESEM FEG XL 30. The powdered zeolites were pressed as pellets with smooth surface and pasted on carbon discs. A beam voltage of 15 keV and the carbon coating were used. Typically, the EDS analysis was conducted on three different 50 μm × 50 μm areas of each prepared zeolite pellet. The good precision of the EDS method was verified in a previous study [28].

Fourier transformed infrared (FT-IR) spectra were collected in the mid-region (the wavenumber from 3996 to 339 cm^{-1}) on a Bruker Tensor 27 FT-IR spectrometer using the attenuated total reflection (ATR) technique on small amounts of powder. Spectra were corrected with background subtraction and normalized by the maximum absorbance of asymmetrical stretch of Si-O(Si/Al) bounds. The ^{29}Si solid-state nuclear magnetic resonance measurements using magic-angle spinning (MAS NMR) were performed on the cement/clay samples using a Bruker Avance III NMR spectrometer. A 7 mm CP/MAS probe at 79.5 MHz was used in the ^{29}Si MAS NMR experiments and the following parameters were applied: 4500 Hz sample rotation rate, 20 s relaxation delays, RF field strength of 33.3 kHz during SPINAL64 proton decoupling. The chemical shifts of the ^{29}Si MAS NMR spectra were referenced to an external sample of tetramethylsilane (TMS, Aldrich) with a ^{29}Si chemical shift at −2.3 ppm. A Gaussian lineshape was used for the spectrum deconvolution and the quantification of the ^{29}Si resonance performed by non-linear least-square fits using the software "DMFIT" developed by [37].

2.6. Thermodynamic modelling

Thermodynamic modelling was carried out using the Gibbs free energy minimization program GEM-Selektor v3.3 [38], a powerful geochemical modelling code that computes the equilibrium speciation and the amount of both aqueous and solid phase in a complex chemical system using Gibbs free energy minimization algorithms. The cement database Cemdata'18 [39], completed with the C-N-A-S-H model from [40], was used for cement minerals. Data for albite were taken from the SUPCRT database [41] and data for Na-based zeolites from [28]. Regarding the thermodynamic date for other general aqueous, solid, and gaseous species, the PSI-GEMS thermodynamic database [42] was included. To draw the predominance diagrams for the cement-zeolite-clay system, the PHREEQC [25] and PhreePlot codes [43], coupling with the PHREEQC database version of Cemdata'18, the thermodynamic data for clay minerals in the THERMOCHIMIE database [22], and the currently generated thermodynamic data of zeolites, were employed. The thermodynamic data of the selected solid phases from SUPCRT and the solubility products from THERMOCHIMIE are expected to be consistent with Cemdata'18 database. The "hunt and track" algorithm (i.e., ht1) was used for finding field boundaries of most abundant minerals.

The activity (in mol kg^{-1} H_2O) of a species i, {i}, was calculated from the measured concentrations considering the formation of different aqueous complexes. The activity corresponds to $\{i\} = \gamma_i \cdot m_i$, where γ_i is the activity coefficient and m_i is the concentration in mol kg^{-1} H_2O. The activity coefficients of the aqueous species γ_i were computed with the built-in extended Debye-Hückel equation with common ion-size parameter a_i = 3.31 Å for Na^+ and common third parameter b_y according to the Eq. (1):

$$\log \gamma_i = \frac{-A_y z_i^2 \sqrt{I}}{1 + B_y a_i \sqrt{I}} + b_y I \quad (1)$$

where z_i denotes the charge of species i, I the effective molal ionic strength, b_y is a semi-empirical parameter (~0.098 for NaOH electrolyte at 25 °C), and A_y and B_y are P,T-dependent coefficients. This activity correction is applicable up to ~1 M ionic strength [44].

The activities of the aqueous species, i.e., {Na^+}, {K^+}, {Ca^{2+}}, {Mg^{2+}}, {AlO_2^-}, {SiO_2^0}, {Cl^-}, and {NO_3^-}, were generated based on the measured aqueous species concentrations. According to the corresponding stoichiometric numbers of zeolites, these activities were used to calculate the K_{sp} values for zeolites at 20, 50, 60, and 80 °C.

From the solubility products calculated at different temperatures, the Gibbs free energy of reaction, $\Delta_r G^\circ$, the Gibbs free energy of formation, $\Delta_f G^\circ$, and the entropy, S°, at 25 °C can be obtained according to Eqs. (2), (3):

$$\Delta_r G^0 = \Sigma_i \nu_i \Delta_f G^0 = -RT \ln K_{sp} \quad (2)$$

$$\Delta_a G_T^0 = \Delta_f G_{T_0}^0 - S_{T_0}^0 (T - T_0) + \int_{T_0}^{T} C_P^0 dT - \int_{T_0}^{T} \frac{C_P^0}{T} dT \quad (3)$$

Since $C_p{}^0 = a_0 + a_1 T + a_2 T^{-2} + a_3 T^{-0.5}$ [45], then,

$$\Delta_a G_T^0 = \Delta_f G_{T_0}^0 - S_{T_0}^0 (T - T_0) - a_0 \left(T \ln \frac{T}{T_0} - T + T_0 \right) - 0.5 a_1 (T - T_0)^2 - a_2 \frac{(T - T_0)^2}{2T - T_0^2} - a_3 \frac{2(\sqrt{T} - \sqrt{T_0})^2}{\sqrt{T_0}} \quad (4)$$

where the apparent Gibbs free energy of formation, $\Delta_a G_T{}^0$, refers to the free energies of the elements at 298 K. ν_i are the stoichiometric reaction coefficients, R = 8.31451 J mol^{-1} K^{-1}, T the temperature in K and $C_p{}^0$the heat capacity. a_{0-3} are empirical parameters defined for each mineral. A constant $C_p{}^0$ ($=a_0$) and $a_1 = a_2 = a_3 = 0$ were assumed for the newly derived data for zeolite as only a narrow temperature range had been studied. A more detailed description of the derivation of the dependence of the Gibbs free energy on temperature is given in [18,46].

The saturation index (SI) of a specific solid was calculated from the ion activity product (IAP) based on the measured concentrations in solution according to the Eq. (5):

$$SI = \log \frac{IAP}{K_{sp}} \quad (5)$$

where IAP represents ion activity product and K_{sp} theoretical solubility product of the solid. Once the saturation index is above zero, the solution is oversaturated by the corresponding solid phase, indicating this phase could possibly precipitate. The SI calculation helped to predict

and verify which solid phase could be formed in the complex chemical system.

The standard molar volume (V^0) was calculated based on the PDF reference card for each zeolite. The temperature range (20–80 °C) of the measured log K_{sp} values is too narrow to determine the standard heat capacity reliably. Thus the C_p^0 values for the zeolites were selected from experimentally measured C_p^0 values in literatures; if not available, they were estimated using the additivity method [17,18] based on a reported experimental C_p^0 value of zeolite having the same framework and/or on the elementary (hydro)oxide components assuming $\Delta C_{p,r} = 0$. Also the entropy values were taken if possible from the literature; if not available, they were determined independently by fitting the log K_{sp} data as a function of temperature with the assistance of the GEMS-Selektor code, or calculated from structurally similar zeolites according to the procedure outlined in [41]. The entropy of a phase A was calculated from the entropy of the solids B and C assuming $\Delta S_r = 0$ considering the molar volume according to Eq. 62 in [41]: $S_A = (S_B + S_C)\cdot(V_B^0 + V_C^0 + V_A^0)/2/(V_B^0 + V_C^0)$. For the additivity method, the thermodynamic data of the elementary (hydro)oxide components (i.e., NaOH, $Ca(OH)_2$, KOH, $Al(OH)_3$, SiO_2, NaCl, $NaNO_3$, and Na_2CO_3) was extracted from [47,48] and summarized in Table A1. Instead of free H_2O, zeolitic H_2O was adopted in the calculation, which gives the S^0 and C_p^0 values of 59.0 and 47.7 J mol^{-1} K^{-1}, respectively [41].

3. Results and discussions

3.1. Characterizations of Ca-based zeolites

3.1.1. Mineralogical compositions

The fine (through 63 μm sieves) grinded zeolite powders were measured by XRD to check their purities and any possible competing crystalline phase. Six framework types (i.e., CHA, GIS, MOR, NAT, STI, and HEU) of the Ca-based zeolites were identified and their high purity verified by XRD. As shown in Fig. 1, almost no impurity diffraction peak was visible for both synthesized (Ca-exchanged CHA(Ca), LS-P(Ca), and MOR(Ca)) and natural (SCO, STI, CLI, HEU_1, and HEU_2) zeolites, except for CHA(Ca) which contained a tiny amount of SiO_2 impurity. For each XRD pattern, the identified mineralogical composition with PDF reference card number is indicated on the top right.

Table 1
Atomic percentages of selected elements of zeolites. The ratio of positive extra-framework charge number to negative framework charge number (Cat/Al) was calculated and the molar ratio of Si to Al listed as well.

Zeolite	Na %	Al %	Si %	K %	Ca %	Mg %	Cat/Al	Si/Al
CHA(Ca)		6.76	13.16	0.48	3.07		0.98	1.95
LS-P(Ca)		10.54	10.29		5.33		1.01	0.98
MOR(Ca)	0.60	2.82	22.22		1.16		1.03	7.86
SCO		8.25	11.95		4.14		1.00	1.45
STI	0.45	5.49	16.80		2.46		0.98	3.06
HEU_1	0.58	5.43	16.31	0.24	2.15		0.94	3.00
HEU_2	0.68	5.43	16.86	0.06	2.20		0.95	3.10
CLI		4.97	23.84	0.92	1.61	0.49	1.03	4.80
Error[a]	7	2	2	7	5	1	7	3

[a] Estimated from three times repetitions of EDS measurements.

3.1.2. Elemental fractions by EDS analysis

In order to crosscheck the chemical formulas obtained from XRD, SEM-EDS analysis was conducted to determine the elemental fractions. The atomic percentages of relatively heavy elements ($Z \geq 11$) were listed in Table 1. The molar ratio of the positive extra-framework charge number to the aluminum substitution, represented by Cat/Al, should be equal to one in a perfect aluminosilicate zeolite structure. As shown in Table 1, almost all the Cat/Al values were approximately equal to 1 (± 0.06). CHA(Ca) and MOR(Ca), two of the cation exchanged zeolites, still contained small fractions of the previous host cation (i.e., K^+ and Na^+, respectively), suggesting that a few cation sites were probably not exchanged by Ca^{2+}. In all the natural zeolites, except for SCO, various cations co-existed in cages but Ca^{2+} always predominated. In addition, the Si/Al ratios of MOR(Ca), STI, HEU_1, HEU_2, and CLI determined by EDS analysis had a certain difference with the values derived from XRD. Eventually, we adopted the values from EDS as it is considered more sensitive to Si/Al ratios than XRD. The elemental fractions of CHA(Ca), LS-P(Ca), and SCO obtained from EDS agreed well with those from XRD.

3.1.3. Water content and possible carbonation

All the zeolite powders were also characterized by TGA-DTG

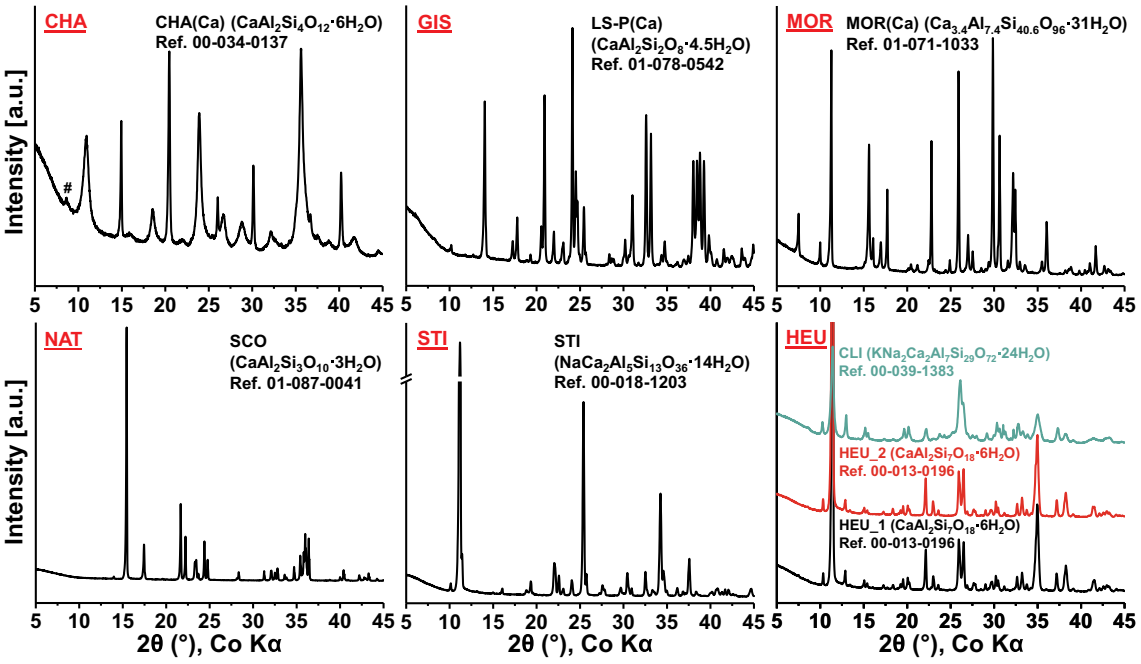

Fig. 1. Powder XRD patterns of the synthesized and natural Ca-based zeolites. Only are the diffraction peaks of impurities marked with symbols, while all the other peaks are attributed to the pure zeolite phases. #: SiO_2 (PDF ref. 00–045-0130).

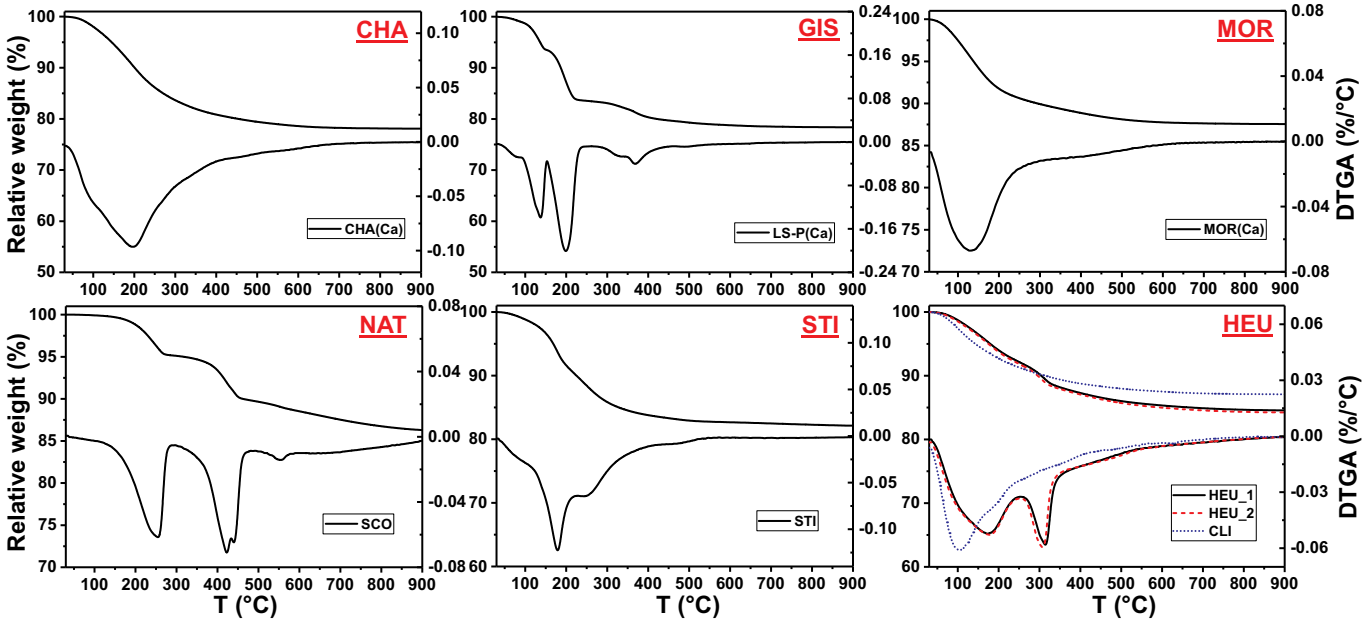

Fig. 2. TGA-DTG curves of the synthesized and natural Ca-based zeolites.

analysis, in order to quantify the water content and to check any possible carbonation during the synthesis. As shown in Fig. 2, the TGA-DTG curves of the Ca^{2+}-exchanged synthesized zeolites (i.e., CHA(Ca), LS-P(Ca), and MOR(Ca)) had little difference with their as-synthesized Na^+/K^+-endmembers [28]. The structure of SCO is similar to that of natrolite ($Na_2Al_2Si_3O_{10}{\cdot}2H_2O$), with a well-ordered Si/Al framework, Ca instead of Na, and an extra molecule of H_2O. Its H_2O molecules can occupy the vacant cation positions and be around the extra-framework Ca^{2+}, probably resulting in the two major peak ranges of water loss. The natural STI contained both zeolitic and crystal water, and the water molecules were coordinated with Ca^{2+} and Na^+ ions. Regarding HEU zeolites, the sharp peak at ~310 °C during a broad thermal reaction of dehydration was the thermogravimetric characteristic of heulandite, as some of the water molecules are closer to calcium than others weakly held water molecules [49]. Clinoptilolite is defined as the series with the similar framework as heulandite, but the Si/Al ratio is above 4.0. XRD is not suitable for separating clinoptilolite and heulandite, but TGA analysis is adequate. As shown in Fig. 2, no carbonation was detected for all the zeolites. Overall, the experimental relative weight losses of CHA(Ca), LS-P(Ca), and SCO were in accordance with the theoretical values based on the chemical formulas (Table 2).

Table 2
Summary of the theoretical relative weight loss of each zeolite and the experimentally obtained values from TGA-DTG analysis. Temperatures of the main DTGA peaks were listed as well.

Zeolite	Theoretical relative weight loss	Experimental relative weight loss/DTGA peak position
CHA(Ca)	21.3%	21.8%/196 °C
LS-P(Ca)	22.6%	21.2%/137, 199, 337, 368, 484 °C
MOR(Ca)	–	12.4%/129 °C
SCO	13.8%	13.6%/255, 423, 440, 554
STI	–	17.3%/179, 244 °C
HEU_1	–	12.0%/176, 314 °C
HEU_2	–	12.3%/176, 308 °C
CLI	–	12.8%/103 °C

3.1.4. FT-IR analyses

FT-IR transmittance spectra and the corresponding 2nd derivative spectra of the zeolites, with wavenumbers ranging from 1400 to 340 cm^{-1} were shown in Fig. 3. The vibration features of the aluminosilicate frameworks of zeolites are mainly displayed in the mid and far infrared, especially below 1400 cm^{-1}. The spectra in the wavenumber range from 4000 to 1250 cm^{-1} (Fig. A2) typically showed the stretching and bending vibration bands of H-O-H (in H_2O) at ~3350 and 1630 cm^{-1}, respectively, with the former giving a broad peak envelop and the latter a sharp peak. A summary of the vibration peak wavenumbers of FTIR spectra is shown in Table 3. According to the assignment theory of [50], the IR transmittance bands can be generally separated into two groups: 1) internal vibrations of the TO_4 tetrahedra (i.e., SiO_4 or AlO_4), including asymmetrical stretch (ν_{as}) in 1250–920 cm^{-1}, symmetrical stretch (ν_s) in 720–650 cm^{-1}, and T-O bend (δ) in 500–420 cm^{-1}; 2) external vibrations of linkages, including ν_{as} in 1150–1050 cm^{-1}, ν_s in 820–750 cm^{-1}, ring vibrations in 650–500 cm^{-1}, and pore opening vibrations in 420–300 cm^{-1}. The zeolites having the same framework of HEU resulted in very similar features in their IR spectra, indicating that the framework vibrations of zeolites can be sensitively detected with these IR bands. Overall, the wavenumbers of the main IR bands for each framework were in good agreement with the literature values [51,52], indicating that the targeted zeolites were collected successfully.

3.1.5. Experimentally determined chemical formulas

The precise chemical formula of each zeolite was challenging to determine, as each type of zeolite frameworks can have a high structural variability of Al/Si ratios and cations. Some possible defects of the aluminosilicate frameworks can result in largely varying Al/Si ratios and are difficult to be identified and quantified. Besides, the mixing or doping of various extra-framework cations is also common for some framework types [53,54], especially in the case of natural zeolites. Therefore, a combination of different characterization techniques was needed to identify all the factors that could visibly influence the solubility products and thus the thermodynamic properties of zeolites. In this work, by using the different characterization methods, the experimental chemical formulas of different zeolites were determined to be CHA(Ca): $Ca_{0.93}K_{0.14}Al_2Si_4O_{12}{\cdot}6H_2O$, MOR(Ca): $Ca_{0.27}Na_{0.14}Al_{0.68}Si_{5.32}O_{12}{\cdot}2.9H_2O$, HEU_1: $Ca_{0.90}Na_{0.25}K_{0.09}Al_{2.14}Si_{6.86}O_{18}{\cdot}4.4H_2O$, HEU_2: $Ca_{0.92}Na_{0.28}K_{0.02}Al_{2.14}Si_{6.86}O_{18}{\cdot}4.5H_2O$, STI: $Ca_{1.02}Na_{0.18}Al_{2.22}Si_{6.78}O_{18}{\cdot}6.8H_2O$, and CLI: $Ca_{0.33}K_{0.18}Mg_{0.10}Al_{1.04}Si_{4.96}O_{12}{\cdot}3.1H_2O$, respectively. These experimentally derived chemical formulas were used to calculate the

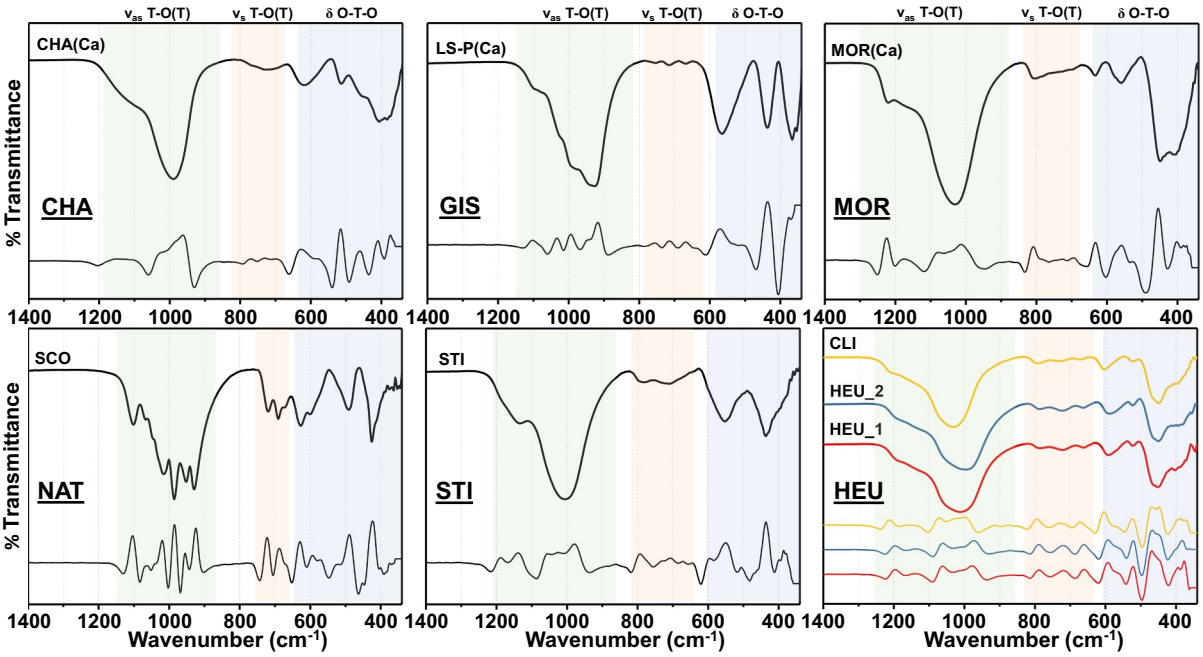

Fig. 3. FTIR transmittance spectra of each type of zeolite framework, with the corresponding 2nd derivative spectra plotted below.

total number of the TO_4 tetrahedra within each aluminosilicate framework and further to calibrate the molar volumes (Table 4).

3.2. Solubility products and derived thermodynamic data

The log K_{sp} values of the studied zeolites at different equilibrium temperatures were listed in Table A2, together with the aqueous concentrations and pH values. In general, for each zeolite the concentrations of dissolved AlO_2^- and SiO_2, i.e., $[Al]_{tot}$ and $[Si]_{tot}$, increased with temperature, resulting in the increase of log K_{sp} values. However, exceptions were observed for $[Ca]_{tot}$, in some cases $[Ca]_{tot}$ decreased with temperatures.

Thermodynamically the zeolites with mixing cations in cages can be treated as solid solutions, single solid, or end members with the main single cations. According to the three models, the Lippmann's total solubility product (ΣΠ) and Ksp values of each zeolite were calculated ([55,56], see details in Text A1) and plotted in Fig. A3. We found that the value from the end member of the main cation was almost equal to that from the solid solution, while the values given by single solid hypothesis and by the end members of the minor cations deviated largely with each other. It suggested that zeolites with various extra-framework cations can be treated as solid solutions more reasonably, rather than single solid structures or separated solid phase with each single cation. As shown in Fig. A3, the log K_{sp} value calculated by solid solution model for the actual composition (with the minor cations) was nearly equal to that for Ca^{2+} end member. Therefore, we adopted their Ca^{2+} end member forms in this thermodynamic study (Table 4).

Based on the log K_{sp} values at different temperatures, the thermodynamic data, including log K_{sp}, $\Delta_f G^0$, $\Delta_f H^0$, and S^0 values, of the zeolites at 25 °C were computed out using GEMS and shown in Table 4. The standard molar volume (V^0) was calculated based on the PDF reference card of each zeolite (Fig. 1). Within the same aluminosilicate framework, the total number of the TO_4 tetrahedra (i.e., AlO_4 and SiO_4) corresponding to a specific chemical formula determines the molar volume, which was already calibrated in Table 4 with the total numbers derived experimentally (see Section 3.1.5).

Thermodynamic properties of selected zeolites in literatures were reviewed and listed in Table 5. As shown in the table, only a few solubility products were obtained experimentally. In addition, the log K_{sp} values can have even several log units difference for the same zeolites. Many factors can cause the large discrepancies, such as different acquiring approaches (experimental vs. theoretical) and inhomogeneous qualities (e.g., purity and crystallinity) of the selected zeolites in literatures. In Fig. 4, the log K_{sp} values of several selected zeolites were compared with the literature values.

For CHA(Ca), the currently generated log K_{sp} values were between the data obtained experimentally by [13] in the presence of Na^+ and Ca^{2+} and the data derived by [21]. The increasing tendency of log K_{sp} values with temperature agreed well with literature values [21], indicating that the S^0 and C_p^0 from literatures describe the experimental log K_{sp} reasonable. By employing the aqueous data of AlSiE50 and AlSiE80 reactors in which CHA(Ca) formed (see Section 3.3), the IAPs of CHA(Ca) in the two reactors were calculated. After ~6 years the IAPs were even larger than those after ~3 years and all the values from the $NaAlO_2$-SiO_2-ettringite systems were larger than those from the zeolite dissolution experiments. It was likely that the aqueous concentrations in the AlSiE reactors were still controlled by the dissolution of materials with larger solubility (e.g., the raw material of silica fume) rather than by CHA(Ca) dissolution.

For the GIS zeolites, our experimental data for LS-P(Ca) are located between the data [21] estimated for synthetic zeolite P(Ca) and for gismondine (natural mineral). The currently generated log K_{sp} curve fitted well with the experimental data at 25 °C from [59], while our oversaturation data started to deviate from the data by Atkins et al. with increasing temperature. Although at 80 °C our current data matched well with the experimental data from [13], their change tendencies of log K_{sp} values with temperature were opposite. After the comparisons, the S^0 value derived experimentally from the LS-P(Ca) dissolution experiment was chosen. Similarly, the log K_{sp} values of LS-P (Ca) generated from albite-ettringite-CSH systems in which LS-P(Ca) formed were plotted in Fig. 4b as well, showing 2–3 log units larger than the LS-P(Ca) dissolution data but having the same positive correlation with temperature with the dissolution data. We assumed that the aqueous concentrations in the cement/rock systems should be controlled by solid phases with higher solubility compared to LS-P(Ca) or the chemical interactions in the systems did not reach equilibrium after ~6 years.

No experimentally determined literature log K_{sp} value is available

Table 3
Summary of the vibration peak wavenumbers (cm^{-1}) of FTIR spectra for the zeolites[a].

Zeolite	Framework	ν O-H	δ O-H	ν_{as} T-O(T) - Ex	ν_{as} T-O(T) - In	ν_s T-O(T) - Ex	ν_s T-O(T) - In	Ring - Ex	δ T-O - In	Pore - Ex
CHA(Ca)	CHA	3396.0	1641.3	1151.4, 1107.1	1030.0, 962.4	769.6, 731.0	700.1	626.8, 515.0	461.0	410.8, 374.2
LS-P(Ca)	GIS	3330.0	1639.4	1103.2	1033.8, 993.3, 918.1	756.1	713.6, 669.3	570.9	435.9	376.1
MOR(Ca)	MOR	3606.7, 3400.3	1627.8	1078.2	1224.7, 1174.6, 1014.5	808.1		632.6, 559.3, 526.5	455.2	401.2
SCO	NAT	3579.7, 3502.6, 3404.2, 3319.3, 3228.7	1662.6, 1647.1, 1587.3	1103.2, 1062.7	1020.3 985.6, 954.7, 923.8		721.3, 688.6	628.8, 594.0, 570.9, 522.7	489.9, 422.4	
STI	STI	3379.1	1635.6	1137.9, 1055.0	1188.1, 1026.1, 979.8	792.7	705.9, 644.2	596.0, 551.6, 505.3	435.9	399.2, 385.7
HEU_1	HEU	3606.7, 3373.0	1622.0	1137.9, 1062.7	1197.7, 977.9	788.8	721.3, 661.6	594.0, 522.7	468.7	393.4, 376.1
HEU_2		3600.9, 3375.3	1624.0	1137.9, 1060.8	1195.8, 974	788.8	721.3, 661.6	592.1, 520.8	468.7	381.9
CLI		3618.3, 3413.8	1627.8	1072.0	1213.2, 1001.0	794.6	729.0, 671.2	603.7, 522.7	468.7, 447.5	387.7, 370.3

[a] ν_{as}, asymmetric stretching vibrations; ν_s, symmetric stretching vibrations; δ, bending vibrations; T, Si/Al tetrahedron; Ex, external linkage; In, internal tetrahedra; Ring, ring vibrations; Pore, pore opening vibrations.

for MOR(Ca) or CLI with the same extraframework cation and Si/Al ratios. After normalizing to the same total number of TO_4, the calculated log K_{sp} values from [21,26–28,60,61] (Table 5) were plotted in Fig. 4c and d for comparisons. As can been seen, the literature values with the same Si/Al ratio but different extraframework cations were relatively close in both cases of MOR(Ca) and CLI. It indicated that the cation types in cages had little effect on the solubility products of mordenite and clinoptilolite, probably as both the zeolites have quite high Si/Al ratios and thus little cationic sites which could limit the effect of the extraframework cations on the overall solubility [27]. Generally, the mordenite and clinoptilolite in literatures having Si/Al ratios of 4.4–5.4 and 4.3–4.4 (Table 5), respectively, were less soluble than MOR(Ca) and CLI in current work having Si/Al ratios of 7.6 and 4.8, respectively. It suggested that the Si/Al ratio even in the same framework type should have large influence on the solubility behavior of the zeolite. Besides, it seems that zeolites in a certain framework type but with higher Si/Al ratios could have higher solubility.

No solubility data for SCO was reported in literature. Compared with the log K_{sp} of scolecite calculated from calorimetric measurements [57], our directly measured log K_{sp} values in the dissolution experiment of SCO were ~ 7 log units larger (Fig. 4e), which is probably related to the presence of impurities and to the large errors associated with solubility data estimated from calorimetric data.

In addition, HEU_1, HEU_2, and STI had quite similar chemical formulas and resulted in very close solubility products (Fig. 4f), although they have different framework types (i.e., HEU and STI). No experimental log K_{sp} derived from solubility measurements can be found in the literature. The log K_{sp} values calculated from calorimetric measurements [62–66] are listed in Table 5. As can be seen, the log K_{sp} values of heulandites are very divergent. Although the heulandites studied in the literatures have a little difference in chemical compositions (e.g., cation types and Si/Al ratios), the huge discrepancy is beyond the limit caused by the different compositions. For stilbites, a large difference was also obtained on log K_{sp} values that were generated from calorimetry data. It shows that the log K_{sp} values derived from calorimetric data for both heulandite and stilbite do not show a good agreement so far and are also largely different with our solubility-generated log K_{sp} values.

3.3. Characterization of 6-year old cement/rock samples

3.3.1. Aqueous results

After reacting for 6 years, the concentrations of aqueous species in the four reactors were measured by IC. As shown in Table 6, the aqueous species were predominated by Na^+ (from the decomposition of albite or the dissolution of $NaAlO_2$) and by Ca^{2+} and SO_4^{2-} (from the decomposition of ettringite). In both systems, an identical S/L ratio of 6.4 g L^{-1} ettringite was used. Once ettringite dissolved completely following Eq. (6), the total amount of SO_4^{2-} and Ca^{2+} would be 15.3 mM and 30.6 mM, respectively. In all the reactors, [SO_4^{2-}] had already reached the total amount of 15.3 mM and even exceeded the upper limit values, indicating that the ettringite decomposed quite completely and the water volume after 6-year reaction decreased due to the formation of water-rich zeolitic phases and/or a slight water evaporation during the long-time high-temperature reaction. In contrast, Ca^{2+} whose concentrations were expected to be two times of [SO_4^{2-}] was present in lower concentrations than SO_4^{2-}, especially for AlSiE reactors. This suggests that calcium originally from ettringite participated in the new precipitation of Ca-containing phases, like zeolites. Besides, the disappearance of a considerable amount of Na^+ implied the possible incorporation of Na^+ in extra-frameworks of newly formed zeolites.

$$2Ca_6Al_2(SO_4)_3(OH)_{12}\cdot 26H_2O(\text{ettringite}) \rightarrow 6Ca^{2+} + 3SO_4^{2-} + 2Al(OH)_4^- + 4OH^- + 26H_2O \quad (6)$$

Table 4
Standard thermodynamic properties of Ca-based zeolites at 25 °C. An experimental error of 3% was applied on the log K_{sp} values [28].

Zeolite	log K_{sp}	$\Delta_f G^0$ (kJ/mol)	$\Delta_f H^0$ (kJ/mol)	S^0 (J/mol/K)	$C_p{}^0$ (J/mol/K)	V^0 (cm^3/mol)
CHA(Ca) ($CaAl_2Si_4O_{12}{\cdot}6H_2O$)	−31.4 ± 0.9	−7144.01	−7806.74	581[a]	617[a]	247.61
LS-P(Ca) ($CaAl_2Si_2O_8{\cdot}4.5H_2O$)	−23.5 ± 0.7	−5076.03	−5527.74	491[b]	435[c]	157.58
MOR(Ca) ($Ca_{0.34}Al_{0.68}Si_{5.32}O_{12}{\cdot}2.9H_2O$)	−21.6 ± 0.6	−5995.73	−6489.11	386[b]	404[d]	209.72
SCO ($CaAl_2Si_3O_{10}{\cdot}3H_2O$)	−24.7 ± 0.7	−5560.52	−6011.65	367[e]	383[e]	172.42
STI ($Ca_{1.11}Al_{2.22}Si_{6.78}O_{18}{\cdot}6.8H_2O$)	−40.4 ± 1.2	−9944.75	−10,815.6	748[b]	782[c]	327.43
HEU_1 ($Ca_{1.07}Al_{2.14}Si_{6.86}O_{18}{\cdot}4.4H_2O$)	−40.4 ± 1.2	−9353.66	−10,118.6	541[b]	611[f]	317.88
HEU_2 ($Ca_{1.07}Al_{2.14}Si_{6.86}O_{18}{\cdot}4.5H_2O$)	−39.3 ± 1.2	−9371.26	−10,131.2	581[b]	619[f]	317.88
CLI ($Ca_{0.52}Al_{1.04}Si_{4.96}O_{12}{\cdot}3.1H_2O$)	−23.6 ± 0.7	−6151.94	−6642.18	454[b]	449[g]	210.91

[a] Indicated by [13];
[b] This study, calculated from log K_{sp} at different temperatures;
[c] Calculated from [21];
[d] Calculated using additivity method based on the elementary (hydro)oxide components;
[e] Measured by [57];
[f] Calculated from [58];
[g] Calculated from [26]; The log K_{sp} was calculated with respect to the species of $AlO_2{}^-$, Ca^{2+}, SiO_2, and H_2O.

3.3.2. XRD characterizations of the solid phase

Powder XRD patterns of the 6-year old cement/rock solid samples were shown in Fig. 5. Regarding the two AEC reactors, albite was still the predominant solid phase after 6 years reaction. Besides, two types of zeolites, i.e., NAT and LS-P(Ca), were newly formed in both reactors. Larger amount of LS-P(Ca) precipitated at 50 °C while more NAT at 80 °C, indicating that NAT is thermodynamically more stable at higher temperatures. This is in good agreement with the thermodynamic properties of NAT obtained experimentally [28] and with the predominance diagrams showing larger stability domains of NAT at higher temperatures. At both 50 and 80 °C, the presence of small quantity of anhydrite ($CaSO_4$) was observed. Only at 80 °C, the diffraction signal of gypsum was detected, which could form via phase transition from anhydrite [70] during sample preparation and storage at room temperature. In both AlSiE reactors, apart from a small amount of carbonates, the formation of FAU and CHA(Ca) was observed from the XRD results (Fig. 5b). Since the XRD patterns of FAU-X and FAU-Y were quite similar in terms of peak positions and peak area ratios [28], it is difficult to distinguish the two phases based on the XRD peaks here. In the presence of high alkali, Al and Si concentrations, FAU predominated the solid product phase at 50 °C, while CHA predominated at higher reaction temperature.

3.3.3. ^{29}Si MAS NMR results

In the AEC reactors, albite was even after ~6 years the predominant solid phase, which was confirmed by deconvolution of the ^{29}Si MAS NMR data (Fig. 6a). The initially added ettringite and C-S-H were almost completely consumed after 6 years reaction. Moreover, the formation of NAT and LS-P(Ca) at both reactors was detected at the corresponding chemical shifts. In accordance with the XRD results, more LS-P(Ca) formed at 50 °C and more NAT at 80 °C. For AlSiE reactors (Fig. 6b), the newly formed FAU-X predominated the solid product at 50 °C while CHA(Ca), possible generated from FAU-Y phase transformation, predominated at 80 °C. At 50 °C, a small amount of silica fume, about 18.2 ± 10.0% from the NMR spectra simulation (Table A3), was still unreacted, while at 80 °C, almost all the silica fume had reacted. By calculating the ratios of peak area (see detailed simulation results in Table A3), the reaction degrees of albite and silica fume in the two respective systems were obtained. Since the relaxation time T1 of silica fume can be very long, the reaction degree of silica fume could be overestimated. In Fig. A4, the reaction degrees after reacting 3 years were also plotted, showing that the chemical interactions were proceeding between 3 and 6 years. The reaction equilibrium was most probably not reached after the long reaction time. Therefore, formation and possible phase transformation of zeolites can occur further. For instance, the FAU formed in reactor AlSiE50 could transform into more stable CHA in longer-term interactions (e.g., in the environments of radioactive waste repositories), in particular as the solutions were clearly oversaturated with respect to chabazite and natrolite (Table 6).

3.3.4. Thermodynamic predictions in degraded cement/rock system

By using the newly generated thermodynamic data of zeolites (Table 4), the saturation indices of selected zeolites were calculated and shown in Table 6. Generally, our thermodynamic predictions of zeolites in degraded cement/clay system are in good agreement with the experimental observations. For the system containing natural albite, C-S-H, and ettringite (AEC reactors), the positive SI values of LS-P(Ca) and NAT indicated solution (over)saturation with respect to the two types of zeolites, in accordance with the XRD and ^{29}Si NMR results. In the cases of AlSiE reactors, no LS-P(Ca) and NAT was detected but their calculated SI values were also highly positive. It suggests a kinetic hindrance of the formation of LS-P(Ca) and NAT under high alkali, Al and Si concentrations when starting with $NaAlO_2$ and silica fume, under which conditions the formation of FAU and CHA zeolites was favored. Actually, the nucleation and grow of FAU-X seems to be much faster than that of LS-P(Ca), as also observed by [76]. However, the FAU zeolites formed were stable for 6 years. The formation of LS-P(Ca) and NAT in AEC reactors could be faster in the presence of potential nucleation centers or structure directing sites on the surface of natural albite and from the relatively low Al and Si concentrations. A similar disagreement between thermodynamic predictions and experimental observations was found for CHA(Ca) in AEC reactors. Typically, a successful synthesis of low-silica CHA can be achieved by a structure transformation from FAU-Y or by necessarily introducing structure directing agents (SDAs, e.g., TMA-OH) in systems without FAU-Y [29,30]. The occurrence of CHA(Ca) product indicated by the positive SI values was unobserved probably due to a lack of SDAs or FAU-Y. In AlSiE reactors, the formation of CHA(Ca) should result from the transformation of preformed FAU-Y, in accordance with the significantly positive SI values for CHA(Ca). In fact, CHA is considered to be more stable

Table 5
Reviewed thermodynamic properties of zeolites in literatures. Experimental values were marked in bold.

Zeolite	Formula	Log K_{sp} (298.15 K)	ΔG_f^0 kJ/mol	ΔH_f^0 kJ/mol	S^0 J/mol K	C_p J/mol K	Ref
Chabazite(Ca)	$CaAl_2Si_4O_{12}{\cdot}6H_2O$	−34.22		−7824.4	614	643	[21]
	$CaAl_2Si_4O_{12}{\cdot}6H_2O$				640	589	[41]
	$CaAl_2Si_4O_{12}{\cdot}6H_2O$	**−25.80**	**−7111.8**	**−7774.0**	581[a]	617[a]	[13]
Chabazite(Na)	$Na_2Al_2Si_4O_{12}{\cdot}6H_2O$	**−31.9 ± 1.0**	**−7117.55**	−7810.40	552	578	[28]
Gismondine	$CaAl_2Si_2O_8{\cdot}4.5H_2O$	−26.25		−5589.9	371	435	[21]
Zeolite P(Ca)	$CaAl_2Si_2O_8{\cdot}4.5H_2O$	−23.17		−5564.6	397	459	[21]
	$CaAl_2Si_2O_8{\cdot}4.5H_2O$	**−20.30**	**−5057.8**	**−5424.0**	**779**	753	[13]
Zeolite P(Na)	$Na_2Al_2Si_2O_8{\cdot}3.8H_2O$	**−19.6 ± 0.6**	**−4858.72**	**−5314.82**	**374**	384	[28]
Mordenite(Ca)	$Ca_{0.515}Al_{1.03}Si_{4.97}O_{12}{\cdot}3.10H_2O$	−26.48	−6165.4	−6662.2	470.6	443.1	[61]
Mordenite(CaNa)	$Ca_{0.29}Na_{0.36}Al_{0.94}Si_{5.06}O_{12}{\cdot}3.47H_2O$	−30.68	**−6247.6**	**−6756.2**	**486.5**	**484.3**	[60]
Mordenite(Ca)	$Ca_{0.56}Al_{1.12}Si_{4.88}O_{12}{\cdot}3.90H_2O$	**−25.32 ± 0.13**	**−6275.0 ± 3.6**				[27]
Mordenite(Na)	$Na_{0.72}Al_{0.72}Si_{5.28}O_{12}{\cdot}2.71H_2O$	**−22.5 ± 0.7**	**−5954.97**	−6442.54	390	405	[28]
Scolecite	$CaAl_2Si_3O_{10}{\cdot}3H_2O$	−31.27	**−5597.9 ± 5.0**	**−6049.0 ± 5.0**	**367.4 ± 0.7**	**383.8 ± 0.8**	[57]
	$CaAl_2Si_3O_{10}{\cdot}3H_2O$		−5597.6	−6049	367.4		[47]
Natrolite	$Na_2Al_2Si_3O_{10}{\cdot}2H_2O$	**−26.6 ± 0.8**	**−5305.15**	−5707.02	360	359	[28]
Stilbite	$CaNa_{0.5}(Al_{2.5}Si_{6.5})O_{18}{\cdot}8H_2O$	−49.06	**−10,347.1**	**−11,289.9**	**811**	**848**	[62]
	$Ca_{1.01}Na_{0.12}Al_{2.12}Si_{6.88}O_{18}{\cdot}7.27H_2O$		**−10,130.9 ± 10.9**	**−11,017.9 ± 10.9**			[64]
	$Ca_{1.019}Na_{0.136}K_{0.006}Al_{2.180}Si_{6.820}O_{18}{\cdot}7.33H_2O$	−55.22	**−10,142.0 ± 6.6**	**−11,033.6 ± 6.6**	**805.5 ± 1.6**	**808.7 ± 1.6**	[63]
Heulandite	$Ca_{1.07}Al_{2.14}Si_{6.86}O_{18}{\cdot}6.17H_2O$			−10,667.2	701	719	[21]
	$Na_{2.14}Al_{2.14}Si_{6.86}O_{18}{\cdot}6.17H_2O$			−10,612.9	838	719	[21]
	$Ca_{0.86}Na_{0.37}K_{0.06}Al_{2.14}Si_{6.86}O_{18}{\cdot}6.1H_2O$	−55.06	**−9835.7 ± 8.6**	**−10,656.3 ± 8.6**	**765.0 ± 2.2**		[64]
	$Ba_{0.065}Sr_{0.175}Ca_{0.585}Na_{0.383}K_{0.132}Al_{2.165}Si_{6.835}O_{18}{\cdot}6H_2O$	−29.55	**−9675.7 ± 10.2**	**−10,491.0 ± 10.2**	**767.2 ± 0.8**	**781.0 ± 0.8**	[65]
	$CaAl_2Si_7O_{18}{\cdot}6H_2O$	−45.02	**−9722.3 ± 6.3**	**−10,524.3 ± 9.6**	**783.7 ± 16**		[66]
	$Na_{0.365}K_{0.059}Ca_{0.861}Al_{2.138}Si_{6.860}O_{18}{\cdot}6.17H_2O$				**736 ± 8**	**752 ± 8**	[58]
Clinoptilolite	$Na_{0.56}K_{0.98}Ca_{1.50}Mg_{1.23}(Al_{6.7}Fe_{0.3})Si_{29}O_{72}{\cdot}22H_2O$				**2872.3 ± 9.0**	**2986.5**	[67]
Clinoptilolite(Ca)	$Ca_{0.56}Al_{1.12}Si_{4.88}O_{12}{\cdot}3.90H_2O$	−27.51		−6923.3	499	481	[21]
Clinoptilolite(Na)	$Na_{1.10}Al_{1.10}Si_{4.90}O_{12}{\cdot}3.50H_2O$	**−26.47**	**−6267.9**	**−6782.4**	**503**	470[b]	[26]
Clinoptilolite(K)	$K_{1.10}Al_{1.10}Si_{4.90}O_{12}{\cdot}2.70H_2O$	**−28.11**	**−6107.4**	**−6568.4**	**508**	454[b]	[26]

[a] Recalculated for $CaAl_2Si_4O_{12}{\cdot}6H_2O$ from the values measured by [68] for natural chabazite;
[b] Estimated from [69]; The log K_{sp} was calculated with respect to the species of AlO_2^-, Na^+, K^+, Ca^{2+}, Sr^{2+}, Ba^{2+}, SiO_2, and H_2O.

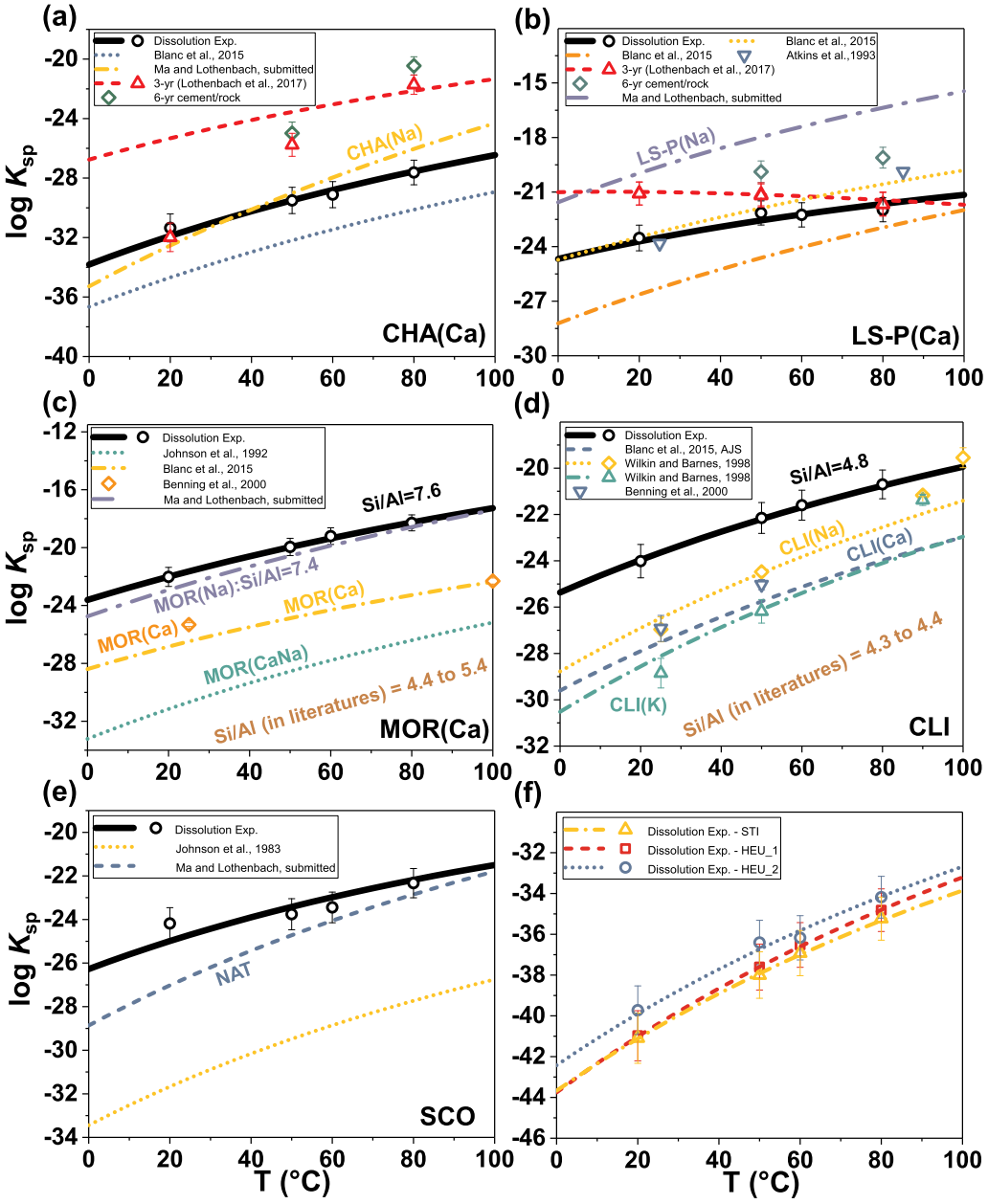

Fig. 4. Solubility products for (a) CHA(Ca), (b) LS-P(Ca), (c) MOR(Ca), (d) CLI, (e) SCO, and (f) STI and HEU. For comparison, solubility products or the relevant curves with temperature in literatures [13,21,26–28,59–61] were also plotted. The chemical compositions of zeolites that were studied by dissolution experiments and that were collected from literature for comparison were shown in Table 4 and Table 5, respectively.

thermodynamically than FAU in hyperalkaline conditions [77]. At higher temperature (i.e., 80 °C) and with longer reaction time, almost pure CHA(Ca) phase was formed, instead of FAU type zeolites, confirming that CHA(Ca) is thermodynamically more stable.

Our experimentally derived thermodynamic data of zeolites was verified preliminarily based on the simple thermodynamic calculations. Although all the formed zeolites in the degraded cement/rock system were successfully confirmed with thermodynamic predictions (i.e.,

Table 6
Aqueous concentrations measured and the calculated SI values of several selected zeolites in the batch experiments of cement/rock interactions. IC measurement error was ± 10%. Thermodynamic data in Table 4 was employed in SI calculations. SI values in cases where the corresponding zeolites were experimentally observed were marked in bold.

ID	pH 25 °C	$[Na]_{aq}$ mM	$[K]_{aq}$ mM	$[Ca]_{aq}$ mM	$[Si]_{aq}$ mM	$[Al]_{aq}$ mM	$[Cl]_{aq}$ mM	$[S]_{aq}$ mM	SI-LS-P(Ca)	SI-NAT	SI-FAU-X	SI-FAU-Y	SI-CHA(Ca)
AEC50	8.43	8.45	0.023	14.5	1.80	0.001	0.034	18.8	**2.67**	**0.01**	−3.24	−0.01	4.11
AEC80	8.24	11.0	0.089	11.9	3.47	0.002	0.048	18.0	**2.54**	**0.01**	−3.47	−0.45	3.53
AlSiE50	10.27	60.1	0.025	0.079	1.13	0.324	0.051	25.6	4.21	4.96	**2.01**	**4.39**	**4.51**
AlSiE80	10.02	48.3	0.014	0.220	6.80	0.346	0.067	20.0	5.82	6.47	**2.93**	**6.16**	**7.10**

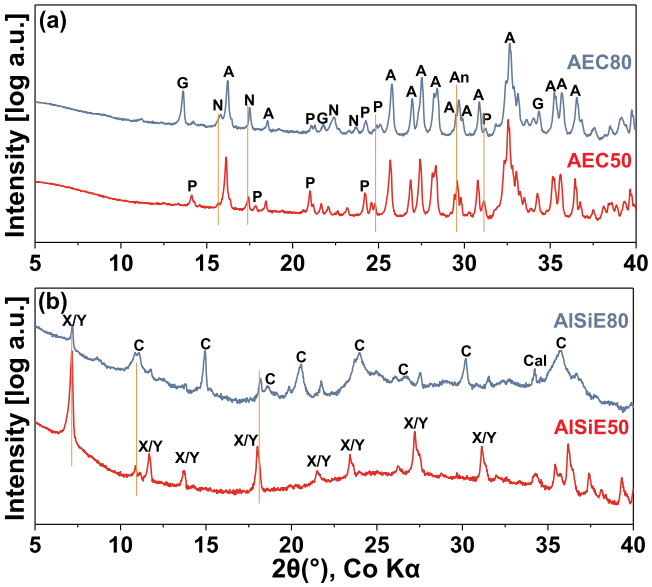

Fig. 5. Powder XRD patterns of AEC samples initially containing albite, ettringite and C-S-H (a) and of AlSiE samples initially containing $NaAlO_2$, SiO_2 and ettringite (b) equilibrated for 6 years at 50 and 80 °C. G: gypsum, An: anhydrite, A: albite, Cal: calcite, N: NAT, P: LS-P(Ca), X: FAU-X, Y: FAU-Y, C: CHA(Ca).

positive SI values), the reverse was not true in all cases as described above. The thermodynamically predicted CHA(Ca) was not detected in AEC reactors while LS-P(Ca) and NAT not in AlSiE reactors. The exceptions can be interpreted by kinetic hindrance, like a lack of necessary seeding, SDA, or precursor zeolitic phases. The use of seeds or SDAs can alter the nucleation process and thus is considered essential for zeolite formation. For instance, seeding or SDA addition is typically a prerequisite for the synthesis of pure NAT, HEU, and ANA [34,54,78]. Once crystals start to grow, activation energies for the growth are considered lower, and crystal growth is faster than nucleation. Therefore, seeding enables a faster crystallization for a pure and particle size controlled zeolite. Besides, the growth kinetics are also strongly dependent on the solution pH, and Al and Si concentrations [79]. Apparently, the kinetic problems affect the experimental observations within a relatively short reaction time. At least, chemical interactions in the simulated degraded cement/rock system did not reach equilibrium even after 6 years according to the ^{29}Si NMR results (Fig. A4). The nucleation and growth kinetics are equally as important as thermodynamic stability in controlling occurrence. The thermodynamic data of zeolites, obtained from a completely independent approach, should provide insights on the stability of zeolites in a geologic time scale, such as in the chemical environment of cementitious nuclear waste repositories.

3.4. Predominance diagrams in cement-zeolite-clay system

Through supplementing the newly generated thermodynamic data of zeolites in Cemdata database, the consistency between cements, zeolites, and clays was examined by establishing their predominance diagrams within chemical environments of $CaO\text{-}SiO_2\text{-}Al_2O_3\text{-}H_2O$. As shown in Fig. 7, no major inconsistency was observed and the stability domain of each solid phase follows the expected sequence. In the sub system saturated with respect to Ca (Fig. 7a and b), portlandite and

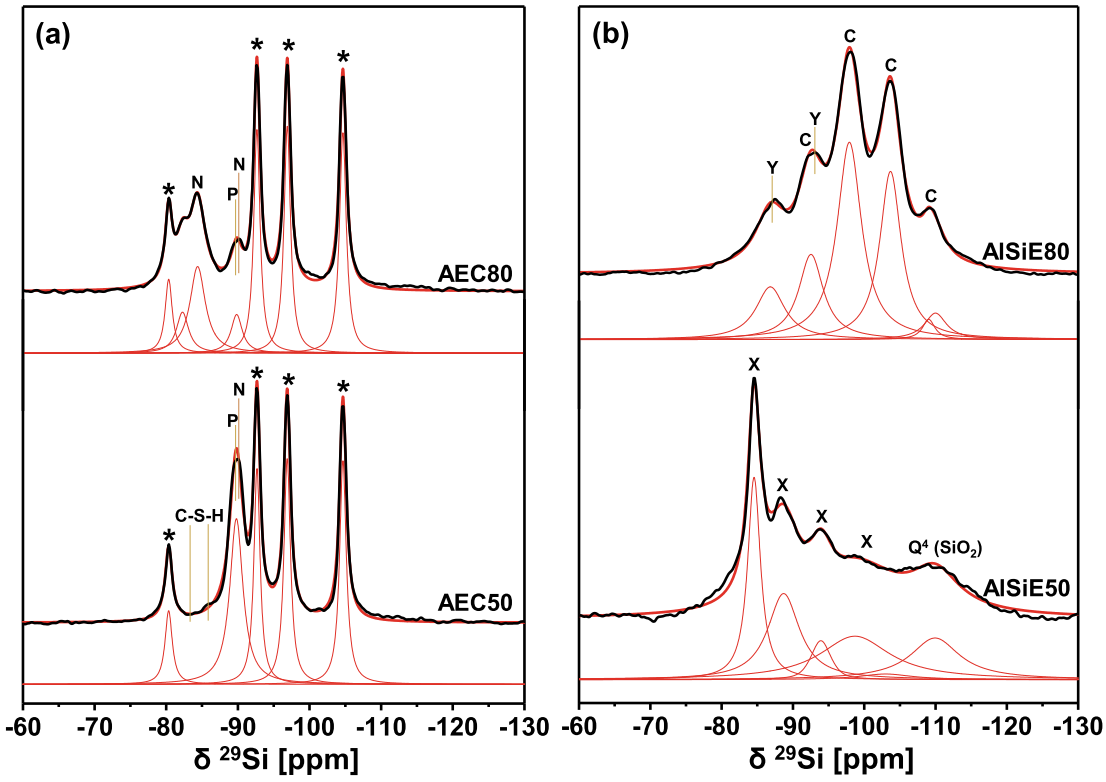

Fig. 6. ^{29}Si MAS NMR spectra of samples initially containing albite, ettringite and C-S-H (a) and of samples initially containing $NaAlO_2$, SiO_2 and ettringite (b) equilibrated for 6 years at 50 and 80 °C. *: albite; C-S-H: calcium silicate hydrate (−83 and −86 ppm [71]); N: natrolite (main signals at −84.4 and −90 ppm [72]); P: LS-P(Ca) (main signal at −89.9 ppm [73]); X: FAU-X (main signals at −84.7 and −89 ppm, less intense signals at −94, −99 and −103 ppm [74]); Y: FAU-Y (main signal at −94.5 ppm, less intense signals at −89, −100 and −105 ppm [74]); C: CHA(Ca) (main signals at −98 and −104 ppm [74]); unreacted SiO_2 at −110 (Q^4) and at −100.9 (Q^3-OH) ppm [75]. Red curves represent the simulation curves for the overall signal and for each component. Black curves are the experimental spectra of samples. (For interpretation of the references to colour in this figure legend, the reader is referred to the web version of this article.)

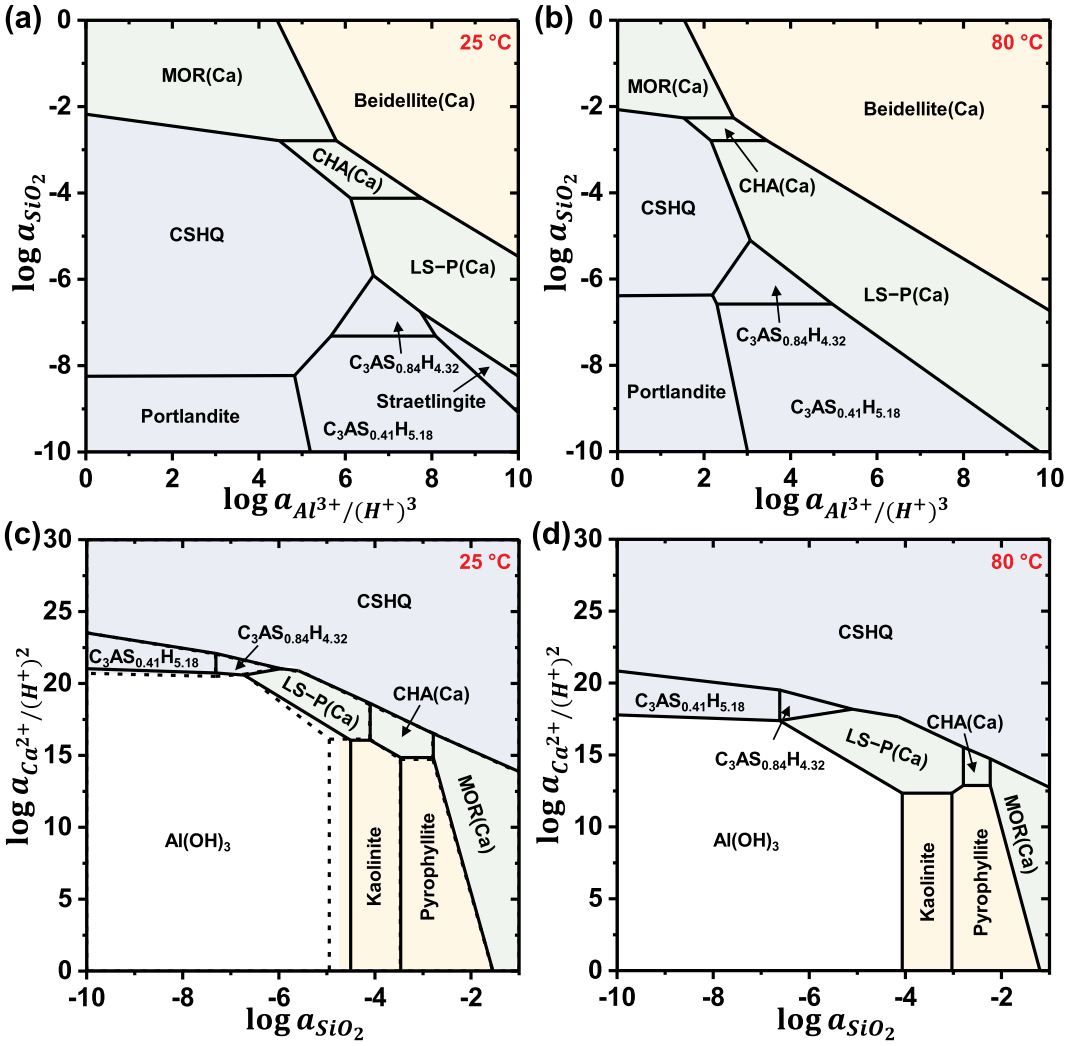

Fig. 7. Predominance diagrams for clay (light yellow), cement (light blue), and zeolite (light green) phases. (a) in CaO-SiO_2-Al_2O_3-H_2O chemical system saturated with respect to portlandite at 25 °C and (b) at 80 °C; (c) in CaO-SiO_2-Al_2O_3-H_2O chemical system saturated with respect to $Al(OH)_3$ at 25 °C and (d) at 80 °C. For Al saturated systems, dash lines indicate the predominant phases with microcrystalline $Al(OH)_3$, while solid lines with gibbsite. (For interpretation of the references to colour in this figure legend, the reader is referred to the web version of this article.)

C(−A)-S-H with relatively higher Ca/Si ratios predominated under highly alkaline conditions. The alkalinity was considered to decrease as [H_4SiO_4] increased. With Si loadings increasing, C-S-H phases were oversaturated. Besides, with high [Al] and high alkalinity, Al-containing cementitious phases, e.g., hydrogarnet and stratlingite, became more stable thermodynamically. In addition, the clay mineral, beidellite(Ca), always occupied the top right part of the diagram, indicating that the clay is stable at low alkaline conditions and high Si and Al concentrations. The part between the stability domains of cements and clays was fully occupied by zeolites. At 25 °C, MOR(Ca) was present under high Si loadings, while low-silica gismondine, LS-P(Ca) predominated in the domain with lower Si/Al ratios. At medium Si/Al ratios, a type of chabazite, CHA(Ca), appeared as a dominant zeolite between CLI and LS-P(Ca). At 80 °C, the area of stability domain of LS-P(Ca) increased to a large extent, suggesting that the formation of gismondine could be more favored at higher temperatures (as expected in the near-field of nuclear waste repositories). MOR, GIS, and CHA types of zeolites are among the most ubiquitous zeolites in nature and have been found in many areas all around the world [53]. In comparison to the results from [21], the thermodynamic property of the current GIS-type zeolite (LS-P(Ca)) was quite similar to the natural gismondine [80], which also resulted in large GIS-type zeolite stability domain in the chemical system.

Regarding the CaO-SiO_2-Al_2O_3-H_2O system saturated with respect to $Al(OH)_3$ (Fig. 7c and d), the stability domains of clays, such as kaolinite and pyrophyllite, were in good agreement with those shown in Fig. 7a and b. Consistently, they were always located in zones of low alkalinity and high [Si]. In between clays and cements, the same types of zeolites were stabilized at each temperature.

4. Conclusions

In this study, two series of simulated cement/rock interaction systems, i.e., systems of albite-ettringite-CSH (AEC) and $NaAlO_2$-SiO_2-ettringite (AlSiE), were investigated, showing that several zeolitic phases, such as gismondine and natrolite in AEC and faujasite and chabazite in AlSiE, respectively, formed after ~6 years interaction. The aqueous results and ^{29}Si MAS NMR spectra indicated that the interaction between cement and rock did not reach equilibrium even after ~6 years.

Reliable thermodynamic data of zeolites based on experimentally determined solubility products were required to predict the stability domains of zeolites in geological time scale. By using hydrothermal cation exchange methods, Ca-based zeolites with framework types of CHA, GIS, and MOR were synthesized. Natural zeolites of scolecite, stilbite, heulandite, and clinoptilolite were also collected for the thermodynamic study. Their framework structures, ratios between extra-

framework cation, Si, and Al, water contents, and low-frequency bonding vibrations were characterized by XRD, EDS, TGA, and FT-IR, respectively. All the solid characterization results indicated that the target zeolites with high purity and homogeneous particle size distribution were synthesized successfully. By carrying out geochemical modelling with GEMS program, thermodynamic data of ΔG_f^0, ΔH_f^0, and S^0 for each zeolite was generated based on the experimental solubility products at 20, 50, 60, and 80 °C. Through the successful thermodynamic prediction of solid products in the independent system of degraded PC/rock interaction, the currently generated thermodynamic data of zeolites was preliminarily verified.

From both independent systems investigated, chabazite and gismondine were expected to be among the thermodynamically stable zeolitic phases in long-term interactions, contrast to intermediate products (e.g., faujasite). Regarding the NAT formation, typically, nucleation centers are necessary and thus the formation kinetics are equally as important as thermodynamic stability in controlling occurrence in nature. In addition, predominance diagrams in the chemical sub-systems of $CaO\text{-}SiO_2\text{-}Al_2O_3\text{-}H_2O$ were established successfully and compared with literature. The derived database for Ca-based zeolites is compatible with the Cemdata18 database and the thermodynamic data of Ca-based clays in the literature. MOR(Ca), CHA(Ca), and LS-P(Ca) were predicted to be the predominant zeolites in the interaction zone between degraded cements and rocks. The experimentally derived thermodynamic data allow predicting zeolite stability domains not only in the context of radioactive waste disposal but also in environments where zeolites could exist. In future, further careful data collations and verifications need to be performed continuously.

This database for Ca-containing zeolites is fully compatible with the cement database Cemdata18 [39] and freely downloadable at http://www.empa.ch/cemdata in formats supporting the computer programs GEM-Selektor [38,81] and in PHREEQC format.

CRediT authorship contribution statement

Bin Ma: Methodology, Investigation, Data curation, Formal analysis, Writing - original draft. **Barbara Lothenbach**: Conceptualization, Supervision, Resources, Writing - review & editing.

Declaration of competing interest

The authors declare that they have no known competing financial interests or personal relationships that could have appeared to influence the work reported in this paper.

Acknowledgements

The authors would like to thank the following funding resources for this research: (a) Distinguished Senior Researcher Grant at Empa, (b) European Union's Horizon 2020 research and innovation programme under the Marie Skłodowska-Curie grant agreement number 754364 and (c) Nagra grant, grant number 16675. Luigi Brunetti is acknowledged for measurements of the ion concentration of the solution, Daniel Rentsch for acquiring all the ^{29}Si MAS NMR spectra, Biwan Xu for SEM-EDS measurements, Yiru Yan for FT-IR acquisitions, Boris Ingold for the lab support, and Frank Winnefeld for help and discussion with XRD measurement and results.

Appendix A. Supplementary data

Supplementary data to this article can be found online at https://doi.org/10.1016/j.cemconres.2020.106149.

References

[1] L. Wang, D. Jacques, P. De Cannière, Effects of an Alkaline Plume on the Boom Clay as a Potential Host Formation for Geological Disposal of Radioactive Waste, External Report SCK·CEN-ER-28, SCK·CEN, Belgium, 2010.
[2] G. Kosakowski, U. Berner, The evolution of clay rock/cement interfaces in a cementitious repository for low- and intermediate level radioactive waste, Phys. Chem. Earth. Parts A/B/C 64 (2013) 65–86.
[3] U.R. Berner, Evolution of pore water chemistry during degradation of cement in a radioactive waste repository environment, Waste Manag. 12 (1992) 201–219.
[4] D. Jacques, L. Wang, E. Martens, D. Mallants, Modelling chemical degradation of concrete during leaching with rain and soil water types, Cem. Concr. Res. 40 (2010) 1306–1313.
[5] M. Ochs, D. Mallants, L. Wang, Radionuclide and Metal Sorption on Cement and Concrete, Springer, 2016.
[6] C. Cau Dit Coumes, S. Courtois, D. Nectoux, S. Leclercq, X. Bourbon, Formulating a low-alkalinity, high-resistance and low-heat concrete for radioactive waste repositories, Cem. Concr. Res. 36 (2006) 2152–2163.
[7] B. Lothenbach, D. Rentsch, E. Wieland, Hydration of a silica fume blended low-alkali shotcrete cement, Phys. Chem. Earth. Parts A/B/C 70-71 (2014) 3–16.
[8] B. Lothenbach, G. Le Saout, M. Ben Haha, R. Figi, E. Wieland, Hydration of a low-alkali CEM III/B–SiO_2 cement (LAC), Cem. Concr. Res. 42 (2012) 410–423.
[9] D. Savage, C. Walker, R. Arthur, C. Rochelle, C. Oda, H. Takase, Alteration of bentonite by hyperalkaline fluids: a review of the role of secondary minerals, Phys. Chem. Earth. Parts A/B/C 32 (2007) 287–297.
[10] E.C. Gaucher, P. Blanc, J.-M. Matray, N. Michau, Modeling diffusion of an alkaline plume in a clay barrier, Appl. Geochem. 19 (2004) 1505–1515.
[11] P. Vieillard, S. Ramírez, A. Bouchet, A. Cassagnabère, A. Meunier, E. Jacquot, Alteration of the Callovo-Oxfordian clay from Meuse-haute Marne underground laboratory (France) by alkaline solution: II. Modelling of mineral reactions, Appl. Geochem. 19 (2004) 1699–1709.
[12] B. Ma, L. Charlet, A. Fernandez-Martinez, M. Kang, B. Madé, A review of the retention mechanisms of redox-sensitive radionuclides in multi-barrier systems, Appl. Geochem. 100 (2019) 414–431.
[13] B. Lothenbach, E. Bernard, U. Mäder, Zeolite formation in the presence of cement hydrates and albite, Phys. Chem. Earth. Parts A/B/C 99 (2017) 77–94.
[14] R. Arthur, H. Sasamoto, C. Walker, M. Yui, Polymer model of zeolite thermochemical stability, Clay Clay Miner. 59 (2011) 626–639.
[15] I. Petrovic, A. Navrotsky, Thermochemistry of Na-faujasites with varying Si/Al ratios, Microporous Mater. 9 (1997) 1–12.
[16] S.V. Mattigod, B.P. McGrail, Estimating the standard free energy of formation of zeolites using the polymer model, Microporous Mesoporous Mater. 27 (1999) 41–47.
[17] R.J. Myers, B. Lothenbach, S.A. Bernal, J.L. Provis, Thermodynamic modelling of alkali-activated slag cements, Appl. Geochem. 61 (2015) 233–247.
[18] G.M. Anderson, D.A. Crerar, Thermodynamics in Geochemistry: The Equilibrium Model, Oxford University Press, 1993.
[19] S.J. Chipera, J.A. Apps, Geochemical stability of natural zeolites, Rev. Mineral. Geochem. 45 (2001) 117–161.
[20] T.S. Bowers, R.G. Burns, Activity diagrams for clinoptilolite; susceptibility of this zeolite to further diagenetic reactions, Am. Mineral. 75 (1990) 601–619.
[21] P. Blanc, P. Vieillard, H. Gailhanou, S. Gaboreau, N. Marty, F. Claret, B. Madé, E. Giffaut, ThermoChimie database developments in the framework of cement/clay interactions, Appl. Geochem. 55 (2015) 95–107.
[22] E. Giffaut, M. Grivé, P. Blanc, P. Vieillard, E. Colàs, H. Gailhanou, S. Gaboreau, N. Marty, B. Madé, L. Duro, Andra thermodynamic database for performance assessment: ThermoChimie, Appl. Geochem. 49 (2014) 225–236.
[23] T.J. Wolery, EQ3NR, a Computer Program for Geochemical Aqueous Speciation-Solubility Calculations: Theoretical Manual, Users Guide, and Related Documentation (Version 7.0), Part 3, Lawrence Livermore National Lab, California, 1992.
[24] E. Shock, P. Canovas, The potential for abiotic organic synthesis and biosynthesis at seafloor hydrothermal systems, Geofluids 10 (2010) 161–192.
[25] D.L. Parkhurst, C. Appelo, Description of Input and Examples for PHREEQC Version 3: A Computer Program for Speciation, Batch-Reaction, One-Dimensional Transport, and Inverse Geochemical Calculations, US Geological Survey, 2013.
[26] R.T. Wilkin, H.L. Barnes, Solubility and stability of zeolites in aqueous solution; I, Analcime, Na-, and K-clinoptilolite, Am. Mineral. 83 (1998) 746–761.
[27] L.G. Benning, R.T. Wilkin, H.L. Barnes, Solubility and stability of zeolites in aqueous solution: II. Calcic clinoptilolite and mordenite, Am. Mineral. 85 (2000) 495–508.
[28] B. Ma, B. Lothenbach, characterization, and thermodynamic study of selected Na-based zeolites, Cem. Concr. Res. 135 (2020) 106111–106129.
[29] D.E. Akporiaye, I.M. Dahl, H.B. Mostad, R. Wendelbo, Aluminum distribution in Chabazite:an experimental and computational study, J. Phys. Chem. 100 (1996) 4148–4153.
[30] R.K. Singh, P. Webley, Adsorption of N_2, O_2, and Ar in potassium Chabazite, Adsorpt 11 (2005) 173–177.
[31] B.R. Albert, A.K. Cheetham, C.J. Adams, Investigations on P zeolites: synthesis and structure of the gismondine analogue, highly crystalline low-silica CaP, Microporous Mesoporous Mater. 21 (1998) 127–132.
[32] B.R. Albert, A.K. Cheetham, J.A. Stuart, C.J. Adams, Investigations on P zeolites: synthesis, characterisation, and structure of highly crystalline low-silica NaP, Microporous Mesoporous Mater. 1 (1998) 133–142.
[33] S.N. Azizi, A. Alavi Daghigh, M. Abrishamkar, Phase transformation of zeolite P to Y and analcime zeolites due to changing the time and temperature, J. Spectro. 2013

(2013) 1–5.
[34] S. Mintova, Verified Synthesis of Zeolitic Materials, third ed., Gulf Professional Publishing, Elsevier, 2016.
[35] L. Wu, A. Navrotsky, Synthesis and thermodynamic study of transition metal ion (Mn^{2+}, Co^{2+}, Cu^{2+}, and Zn^{2+}) exchanged zeolites a and Y, Phys. Chem. Chem. Phys. 18 (2016) 10116–10122.
[36] W.M. Murphy, R.T. Pabalan, J.D. Prikryl, C.J. Goulet, Reaction kinetics and thermodynamics of aqueous dissolution and growth of analcime and Na-clinoptilolite at 25 °C, Am. J. Sci. 296 (1996) 128–186.
[37] D. Massiot, F. Fayon, M. Capron, I. King, S. Le Calvé, B. Alonso, J.-O. Durand, B. Bujoli, Z. Gan, G. Hoatson, Modelling one- and two-dimensional solid-state NMR spectra, Magn. Reson. Chem. 40 (2002) 70–76.
[38] D.A. Kulik, T. Wagner, S.V. Dmytrieva, G. Kosakowski, F.F. Hingerl, K.V. Chudnenko, U.R. Berner, GEM-Selektor geochemical modeling package: revised algorithm and GEMS3K numerical kernel for coupled simulation codes, Comput. Geosci. 17 (2013) 1–24.
[39] B. Lothenbach, D.A. Kulik, T. Matschei, M. Balonis, L. Baquerizo, B. Dilnesa, G.D. Miron, R.J. Myers, Cemdata18: a chemical thermodynamic database for hydrated Portland cements and alkali-activated materials, Cem. Concr. Res. 115 (2019) 472–506.
[40] R.J. Myers, S.A. Bernal, J.L. Provis, A thermodynamic model for C-(N-) ASH gel: CNASH_ss. Derivation and validation, Cem. Concr. Res. 66 (2014) 27–47.
[41] H.C. Helgeson, J.M. Delany, H.W. Nesbitt, D.K. Bird, Summary and critique of the thermodynamic properties of rock-forming minerals, Am. J. Sci. 278 (1978) 1–229.
[42] T. Thoenen, W. Hummel, U. Berner, E. Curti, The PSI/Nagra chemical thermodynamic database 12/07, Nagra Working Report NAB (2014).
[43] D. Kinniburgh, D. Cooper, PhreePlot: Creating Graphical Output with PHREEQC, (2011).
[44] B.J. Merkel, B. Planer-Friedrich, Groundwater Geochemistry: A Practical Guide to Modeling of Natural and Contaminated Aquatic Systems, Springer, Berlin, 2008.
[45] R.G. Berman, Internally-consistent thermodynamic data for minerals in the system Na_2O-K_2O-CaO-MgO-FeO-Fe_2O_3-Al_2O_3-SiO_2-TiO_2-H_2O-CO_2, J. Petrol. 29 (1988) 445–522.
[46] D.A. Kulik, Minimising Uncertainty Induced by Temperature Extrapolations of Thermodynamic Data: A Pragmatic View on the Integration of Thermodynamic Databases into Geochemical Computer Codes, Nuclear Energy Agency of the OECD (NEA), 2002.
[47] R.A. Robie, B.S. Hemingway, Thermodynamic Properties of Minerals and Related Substances at 298.15 K and 1 Bar (10^5 Pascals) Pressure and at Higher Temperatures, 2131 US Government Printing Office, 1995.
[48] M.W.J. Chase, NIST-JANAF thermochemical tables: National Institute of Standards and Technology (fourth edition), J. Phys. Chem. Ref. Data 9 (1998).
[49] M. Földvári, Handbook of the Thermogravimetric System of Minerals and its Use in Geological Practice, Occasional Papers of the Geological Institute of Hungary, (2013) Budapest.
[50] E.M. Flanigen, H. Khatami, H.A. Szymanski, Infrared structural studies of zeolite frameworks, in: E.M. Flanigen, L.B. Sand (Eds.), Molecular Sieve Zeolites-I, Advances in Chemistry, American Chemical Society, 1974, pp. 201–229.
[51] W. Mozgawa, M. Krol, K. Barczyk, FT-IR studies of zeolites from different structural groups, Chemik 65 (2011) 667–674.
[52] J. Scherzer, J.L. Bass, Infrared spectra of ultrastable zeolites derived from type Y zeolites, J. Catal. 28 (1973) 101–115.
[53] G. Glauco, G. Ermanno, Natural Zeolites, Springer, 1985.
[54] P. Ambrozova, J. Kynicky, T. Urubek, V.D. Nguyen, Synthesis and modification of Clinoptilolite, Molecules 22 (2017) 1107.
[55] P.D. Glynn, E.J. Reardon, Solid-solution aqueous-solution equilibria; thermodynamic theory and representation, Am. J. Sci. 290 (1990) 164–201.
[56] S.M. Leisinger, B. Lothenbach, G. Le Saout, C.A. Johnson, Thermodynamic modeling of solid solutions between monosulfate and monochromate $3CaO{\cdot}Al_2O_3{\cdot}Ca[(CrO_4)_x(SO_4)_{1-x}]{\cdot}nH_2O$, Cem. Concr. Res. 42 (2012) 158–165.
[57] G. Johnson, H. Flotow, P. O'Hare, W. Wise, Thermodynamic studies of zeolites; natrolite, mesolite and scolecite, Am. Mineral. 68 (1983) 1134–1145.
[58] V. Drebushchak, V. Naumov, V. Nogteva, I. Belitsky, I. Paukov, Low-temperature heat capacity of heulandite: comparison with clinoptilolite, Thermochim. Acta 348 (2000) 33–40.
[59] M. Atkins, F. Glasser, I. Moron, J. Jack, Thermodynamic Modelling of Blended Cements at Elevated Temperature (50–90 °C). DOE Report: DoE/HIMP/RR/94.011, (1993).
[60] G. Johnson, I. Tasker, H. Flotow, P. O'Hare, W. Wise, Thermodynamic studies of mordenite, dehydrated mordenite, and gibbsite, Am. Mineral. 77 (1992) 85–93.
[61] P. Blanc, P. Vieillard, H. Gailhanou, S. Gaboreau, E. Gaucher, C.I. Fialips, B. Madé, E. Giffaut, A generalized model for predicting the thermodynamic properties of clay minerals, Am. J. Sci. 315 (2015) 734–780.
[62] T. Fridriksson, P.S. Neuhoff, S. Arnórsson, D.K. Bird, Geological constraints on the thermodynamic properties of the stilbite—stellerite solid solution in low-grade metabasalts, Geochim. Cosmochim. Acta 65 (2001) 3993–4008.
[63] D.A. Howell, G.K. Johnson, I.R. Tasker, P.A.G. O'Hare, W.S. Wise, Thermodynamic properties of the zeolite stilbite, Zeolites 10 (1990) 525–531.
[64] I. Kiseleva, A. Navrotsky, I. Belitsky, B. Fursenko, Thermochemical study of calcium zeolites–heulandite and stilbite, Am. Mineral. (2001) 448–455.
[65] G. Johnson, H. Flotow, P. O'Hare, W.S. Wise, Thermodynamic studies of zeolites: heulandite, Am. Mineral. 70 (1985) 1065–1071.
[66] M. Cho, S. Maruyama, J.G. Liou, An experimental investigation of heulandite-laumontite equilibrium at 1000 to 2000 bar Pfluid, Contrib. Mineral. Petrol. 97 (1987) 43–50.
[67] B.S. Hemingway, R.A. Robie, Thermodynamic properties of zeolites: low-temperature heat capacities and thermodynamic functions for phillipsite and clinoptilolite. Estimates of the thermochemical properties of zeolitic water at low temperature, Am. Mineral. 69 (1984) 692–700.
[68] I. Belitsky, S. Gabuda, V. Drebushchak, V. Naumov, V. Nogteva, I. Paukov, Heat-Capacity of Chabasite in the Temperature-Range of 5 to 316 K, Entropy and Enthalpy at Standard Conditions, Rossiiskaya Akademiya Nauk, Savelevskii Per, Moscow, 1982.
[69] P. Vieillard, A predictive model for the entropies and heat capacities of zeolites, Eur. J. Mineral. 22 (2010) 823–836.
[70] A.E. Hill, The transition temperature of gypsum to anhydrite, J. Am. Chem. Soc. 59 (1937) 2242–2244.
[71] E. L'Hôpital, B. Lothenbach, D.A. Kulik, K. Scrivener, Influence of calcium to silica ratio on aluminium uptake in calcium silicate hydrate, Cem. Concr. Res. 85 (2016) 111–121.
[72] P.S. Neuhoff, S. Kroeker, L.-S. Du, T. Fridriksson, J.F. Stebbins, Order/disorder in natrolite group zeolites: a ^{29}Si and ^{27}Al MAS NMR study, Am. Mineral. 87 (2002) 1307–1320.
[73] J.G. Nery, Y.P. Mascarenhas, A.K. Cheetham, A study of the highly crystalline, low-silica, fully hydrated zeolite P ion exchanged with (Mn^{2+}, Cd^{2+}, Pb^{2+}, Sr^{2+}, Ba^{2+}) cations, Microporous Mesoporous Mater. 57 (2003) 229–248.
[74] E. Lippmaa, M. Maegi, A. Samoson, M. Tarmak, G. Engelhardt, Investigation of the structure of zeolites by solid-state high-resolution silicon-29 NMR spectroscopy, J. Am. Chem. Soc. 103 (1981) 4992–4996.
[75] J.-B. d'Espinose de la Caillerie, M. Kermarec, O. Clause, ^{29}Si NMR observation of an amorphous magnesium silicate formed during impregnation of silica with mg(II) in aqueous solution, J. Phys. Chem. 99 (1995) 17273–17281.
[76] A. Katović, B. Subotić, I. Šmit, L.A. Despotović, M. Ćurić, Role of gel aging in zeolite crystallization, in: M.L. Occelli, H.E. Robson (Eds.), Zeolite Synthesis, ACS Symposium Series, American Chemical Society, 1989, pp. 124–139.
[77] L. Van Tendeloo, W. Wangermez, M. Kurttepeli, B. de Blochouse, S. Bals, G. Van Tendeloo, J.A. Martens, A. Maes, C.E.A. Kirschhock, E. Breynaert, Chabazite: stable cation-exchanger in hyper alkaline concrete pore water, Environ. Sci. Technol. 49 (2015) 2358–2365.
[78] J. Shin, N.H. Ahn, M.A. Camblor, C.M. Zicovich-Wilson, S.B. Hong, Synthesis of aluminosilicate natrolites and control of their tetrahedral atom ordering, Chem. Mater. 26 (2014) 3361–3363.
[79] R.J. Donahoe, J.G. Liou, An experimental study on the process of zeolite formation, Geochim. Cosmochim. Acta 49 (1985) 2349–2360.
[80] L.P. Ogorodova, L.V. Mel'chakova, I.A. Kiseleva, I.A. Belitskii, Thermodynamic properties of natural zeolites of the gismondine-harronite group, Russ. J. Phys. Chem. A 77 (2003) 1543–1545.
[81] T. Wagner, D.A. Kulik, F.F. Hingerl, S.V. Dmytrieva, GEM-Selektor geochemical modeling package: TSolMod library and data interface for multicomponent phase models, Can. Mineral. 50 (2012) 1173–1195.